Cryst. Res. Technol. **47**, No. 3, 285 – 292 (2012) / **DOI** 10.1002/crat.201100494

Numerical modelling of Czochralski growth of quadratic silicon crystals by means of a travelling magnetic field

W. Miller*[1], Ch. Frank-Rotsch[1], M. Czupalla[1], and P. Rudolph[2]

[1] Leibniz Institute for Crystal Growth (IKZ), Max-Born-Str. 2, 12489 Berlin, Germany
[2] Crystal Technology Consulting (CTC), Helga-Hahnemann-Str. 57, 12529 Schönefeld, Germany

Received 18 October 2011, revised 24 October 2011, accepted 28 October 2011
Published online 11 November 2011

Key words numerical simulation, Czochralski growth, facets.

We present 3D simulations of melt flow in a Czochralski process of Si single crystal growth with a travelling magnetic field (TMF). The choice of the TMF significantly influences the thermal field in the melt. Using a downwards TMF field the induced convection causes a thermal field with a low radial component of the temperature gradient along the melt surface and a high vertical component below the crystal. Such a thermal field allows the kinetics-based creation of {110} side facets, which was proven in several experimental runs.

1 Introduction

During recent years it has been shown that a travelling magnetic field (TMF) can significantly influence the melt flow and temperature field in Czochralski crystal growth processes [1-3]. This opens a wide field of applying TMFs for various favourable aims, e.g. reducing temperature fluctuations, to enhance mass transport, and others. In this paper we show how the melt flow in a Czochralski process of Si growth can be influenced by a TMF in order to allow the growth of Si crystals with quadratic cross section caused by creation, development and control of four {110} side facets when the crystal is grown in the [00$\bar{1}$] direction. For this purpose we have performed 3D simulations of the melt flow. If a TMF is chosen to counteract the convection roll caused by the crucible rotation and buoyancy convection the radial component of the temperature gradient at the melt surface is reduced and the vertical component beneath the crystal is increased, which leads to the evolution of {110} side facets. Practically, this has been already proven [4]. In these experiments the KRIST*MAG*® concept has been used, i.e. the graphite heater was simultaneously used for the generation of heat and of TMF [3,5]. On the other hand, if a TMF is chosen, which enhances the convection roll caused by the crucible rotation and buoyancy convection the thermal conditions near the melt/crystal interface do not allow the creation of {110} side facets and the crystal grown has the typical cylindrical shape.

2 Geometry and numerical methods

A sketch of the global symmetry and geometry of the 6-inch crucible arrangement is shown in [4]. The sizes of crystal and crucible in the 3 D simulation can be seen in figure 1 from the top view on the domain computed. The height of the melt was 42.1 mm in the centre. In the first step the global temperature field in the furnace is computed by performing axisymmetric (2.5 D) calculations using CrysMAS [6]. This program is also used for the computation of the Lorentz force densities. In the second step the melt flow is computed by 3 D simulations taking into account only the melt and using thermal boundary conditions obtained by the 2.5 D computations. The commercial code Ansys-cfx was used for the 3 D simulations employing the large eddy Smagorinsky

* Corresponding author: e-mail: miller@ikz-berlin.de

model. Details can be found in [7]. We used a rotational coordinate frame in order to let the crystal at rest, because it is not axisymmetric. Thus, we can use a fixed grid. For all computations we had a hexahedral mesh with 931,000 control volumes and a resolution at the boundaries down to 0.12 mm.

A crucial point are the thermal boundary conditions because the global simulation is without any melt convection. In [7] we used heat flux at the crucible wall but temperature at the melt surface. At the flat crystal melt interface we have the melting point temperature by definition.

For the calculations presented in this paper we use heat flux as the thermal boundary condition also at the melt surface in order to be more realistic and allow a temperature variation at the melt surface. Because the main contribution to heat transport in the furnace is by radiation we set the heat flux at node i as $f_i=\alpha\,(T^{ext}{}_i^4 - T_i^4)$, where T_i is the temperature at node i and $T^{ext}{}_i$ the corresponding external temperature. α and $T^{ext}{}_i$ are computed from the heat flux in the case without convection, obtained by the 2.5 D global simulation of CrysMAS. α is computed at one grid point, choosing $T^{ext}{}_i$ = 1350 K. Then $T^{ext}{}_i$ for all other grid points is computed using the obtained value α=-1.794 10^{-8} W/m^2 K^4.

For the thermal conditions at top it has to be taken into account that the data provided by the result of CrysMAS simulations are axisymmetric with a crystal of 94 mm diameter. Thus, the conditions on the melt surface near the facets are not described correctly. Nevertheless, we will see that the results of the computations provide a good insight into the thermal conditions.

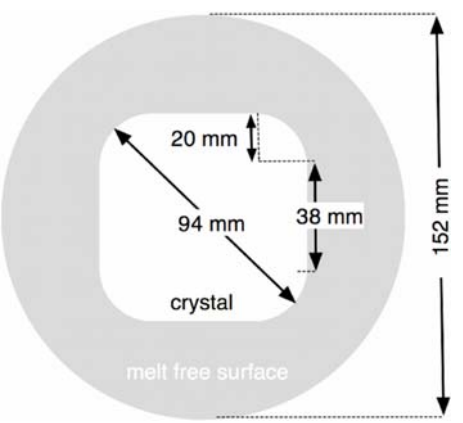

Fig. 1 Top view on geometry. The data correspond to those of the crystal grown.

In the computations we consider buoyancy convection, crystal rotation (15 rpm) and counter rotation of the crucible (5 rpm). Because of the non-axisymmetric shape of the crystal we use a moving reference frame with the crystal rotation rate and apply the Coriolis and the centrifugal force in the melt. We also include Marangoni convection. Due to the strong temperature fluctuations on the melt surface the Marangoni forces act locally in the azimuthal direction. This can be clearly seen in figure 2, where the temperature and velocity on melt surface are shown for a computation without (left) and with Marangoni convection (right). There is a backflow towards the cold spikes on the melt surface. All computations presented in the following have been computed including Marangoni convection.

All physical parameters used in the 3 D computations are listed in table 1. In addition, the characteristic numbers are given, showing that a major contribution from the TMF induced flow on the convection can be expected.

3 Results and discussion

3.1 Numerical simulations We have performed calculations without TMF and with both an upward and with a downward directed TMF. The two latter ones correspond to the experimental conditions. An upward TMF (short: TMF up) means a positive phase shift measured from the topmost side heater and a downward TMF (short: TMF down) means a negative phase shift. The vertical components of the Lorentz forces are

directed in positive z-direction in the first case and in negative z-direction in the second one. In all cases we measured the temperature at three monitoring points at the melt surface (r=0.047, 0.060 0.074 m).

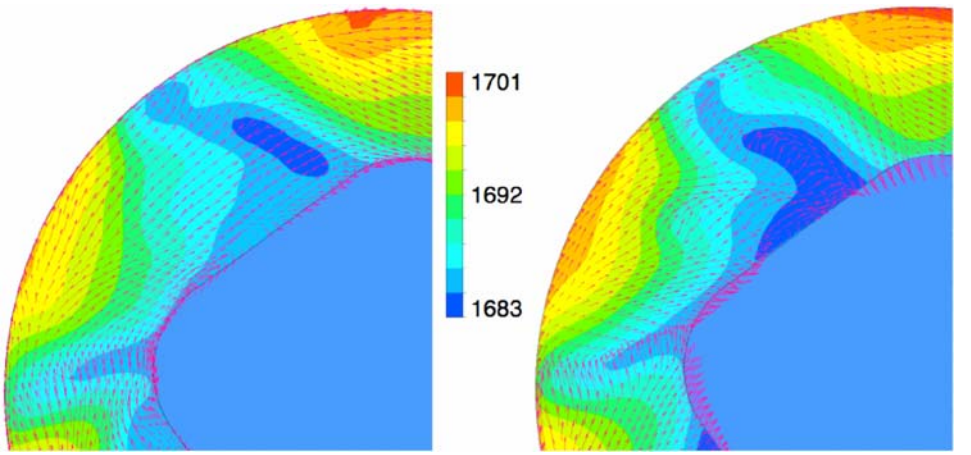

Fig. 2 Temperature profile and velocity vectors for a calculation without TMF when a rectangular crystal cross section is assumed. Left: without Marangoni convection. Right: with Marangoni convection. Both pictures were taken 4.2 s after starting from the situation without convection.

Table 1 Physical parameters used for the computations.

Melting point temperature	T_m	1685 K
Density	ρ	2420 kg/m^3
Specific heat	c_p	1000 J/ (kg K)
Thermal conductivity	λ	60 W/(m K)
Dynamic viscosity	μ	7×10^{-4} Pa s
Thermal expansion factor	α	1.41×10^{-4} 1/K
Gravitational acceleration	g	9.81 m/s^2
Thermocapillary coefficient	σ	-7.4×10^{-5} N/(m K)
Charact. Temperature diff.	$(\Delta T)_c$	39 K
Radius of crucible	r_c	0.047 m
Crystal rotation	Ω_X	15 rpm
Crucible rotation	Ω_c	5 rpm
Re_{buoy}	$g\,\alpha\,\rho^2\,\mu^{-2}\,r_c^3\,(\Delta T)_c$	1.8×10^4
Re_X	$2\pi\,\Omega_X\,r_c^2\,\rho^{-1}\,\mu^{-2}$	1.7×10^4
Re_c	$2\pi\,\Omega_c\,r_c^2\,\rho^{-1}\,\mu^{-2}$	9.8×10^3
Re_L (up 300 Hz)	$(\rho\,\max(F_L)\,r_c^3\,\mu^{-2})^{1/2}$	6×10^4
Re_L (up 180 Hz)	$(\rho\,\max(F_L)\,r_c^3\,\mu^{-2})^{1/2}$	4.5×10^4
Re_L (down 60 Hz)	$(\rho\,\max(F_L)\,r_c^3\,\mu^{-2})^{1/2}$	2×10^4
Ma	$-\sigma\,(\Delta T)_c\,r_c\,\rho\,c_p\,\mu^{-1}\,\lambda^{-1}$	8×10^3

Firstly, we consider the case without TMF. We obtained a rotating five-fold symmetry structure of the temperature profile on the melt surface and an oscillating temperature field in the melt. The temperature distribution at a particular time step can be seen in figure 3, where a cut through the melt and half of the melt surface is presented. Three of the five spikes are visible. These pikes are rotating and for a more detailed analysis we computed the power spectrum at the three monitoring points (see fig. 4 left). The main peak is at 1.125 Hz. Please note that this is measured in the frame of crystal rotation (8.5 rpm or 0.1417 Hz). Since we have a five-fold symmetry we divide 1.125 Hz by 5 and then substract the crystal rotation with the result of 0.0833 Hz, which corresponds exactly to the crucible rotation rate (5 rpm). This means that the rotation of the five-fold structure is governed by the crucible rotation, which is also reflected in the reduction of the main peak at the inner monitor points. Because the main structure of the velocity and temperature field is defined by the interaction of buoyancy convection and that caused by the crucible rotation, there is little influence by the shape of the crystal. For the case with a cylindrical crystal we obtain a quite similar power spectrum (see fig. 4)

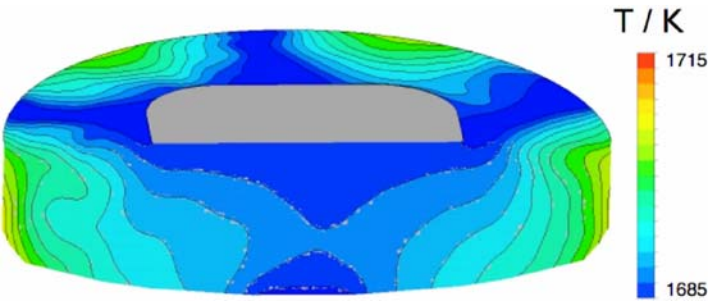

Fig. 3 Case without TMF. Left: instantaneous temperature profile exhibiting a five-fold symmetry at the melt interface.

The situation is completely different when we apply a TMF. The Lorentz forces induced by the TMFs are rather large (maximum F_L=250-2000 N/m^3) and the velocities in the melt are much higher than without TMF (compare also the Reynolds numbers in table 1). Both in experiment and simulation we use the entire electrical current needed for heating also for inducing Lorentz forces.

We have two different situations: when applying a TMF up, i.e. the phase shift is positive counted from the top heater and the resulting vertical component of the Lorentz forces is positive too, we enhance the convection roll caused by the crucible rotation and buoyancy convection. In the opposite case, applying a TMF downwards, we invert the flow direction and have a flow from the crystal to the crucible and an up-streaming in the middle of the melt.

Firstly, we discuss the results for TMF upwards (f=60 Hz). The temperature profile on the melt surface is now rather complex and the corresponding power spectrum broad (see fig. 5). The main peak of the computation without TMF at 1.125 Hz is completely missing and much higher frequencies occur. The heat transport from the wall towards the crystal is enhanced – the convection rolls at the outer part of the melt are clearly pronounced. Consequently, the maximum temperature in the melt is reduced from 1715 K in the case without TMF to 1694 K.

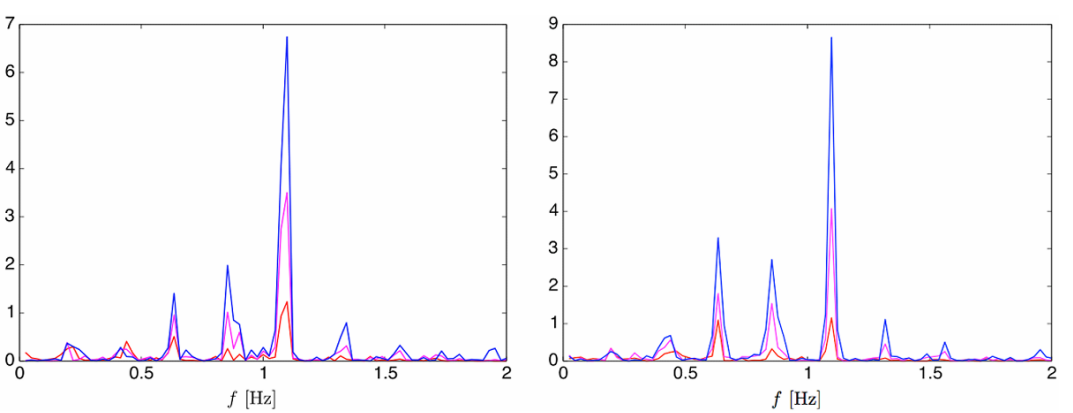

Fig. 4 Power spectra (analysing 48 s) for case without TMF. Left: crystal is square-shaped. Right: crystal is cylindrical. Monitor points: blue (top) r=0.074 m, purple (middle), r=0.060 m , red (bottom) r=0.047 m.

When applying a TMF down 300 Hz the temperature differences in the melt and on the melt surface become rather small and the flow more chaotic. Because of the high velocities (up to 230 mm/s) the computational time step has to be very small (2.5 ms). On the other hand, the frequency spectrum is very broad and very long time series are needed to get any reliable information. At this point we are not interested in the details of the oscillations and therefore we omit the power spectrum analysis.

We are now going to analyse the thermal fields near to the crystal/melt interface in more detail, because they are crucial for the development of {110} side facets and hence for a crystal of nearly quadratic shape. In figure 7 (left) we compare the temperature profiles along the horizontal direction slightly beneath the crystal/melt interface and the melt interface (1 mm below). Using a TMF up the temperature is increasing

sharply beyond the crystal edge, suppressing any formation of facets. Small differences in the temperature profile near to the crystal can be observed by varying the rotation rate of the crucible. The red curve (deeper in the region below the crystal) represents the case with 5 rpm whereas the blue curve represents that with a lower rotation rate of 0.5 rpm.

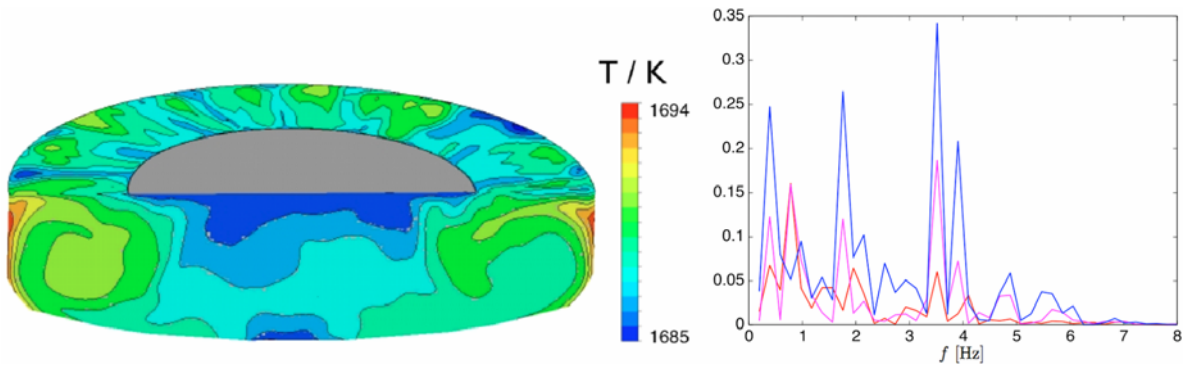

Fig. 5 Case with TMF up. Left: instantaneous temperature profile. Right: Power spectrum (analysing 48 s).

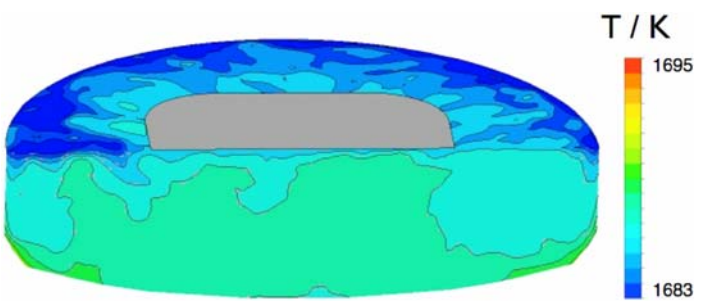

Fig. 6 Case with TMF down. Instantaneous temperature profile.

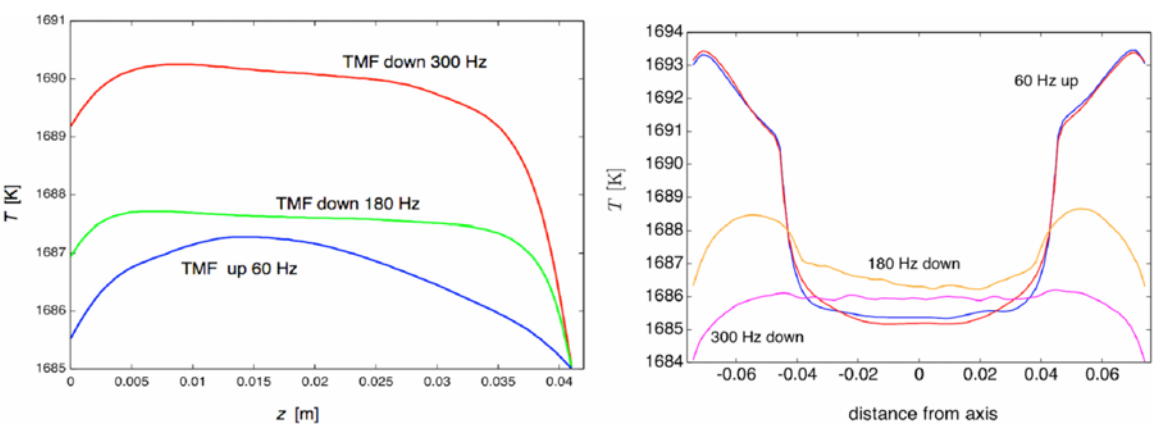

Fig. 7 Left: Time-averaged temperature along horizontal line 1 mm beneath melt surface and melt/crystal interface. The distance is measured in m and the crystal is between -0.039 m and 0.039 m. In cases of TMF up the temperature is steeply increasing towards the crucible, whereas in cases of TMF down the temperature profile is very flat. On the other hand, the vertical component of the temperature gradient below the crystal is higher for a TMF down than for a TMF up. The blue curve for TMF up was obtained with a reduced crucible rotation rate of 0.5 rpm. Right: Time-averaged temperature along central vertical line. The crystal/melt interface is at 0.0421 m.

When using downwards directed TMFs the temperature profile becomes rather flat stabilizing the growth of {110} facets. For a higher frequency the Lorentz forces are higher and the temperatures differences become smaller (compare 180 Hz and 300 Hz). The small temperature differences lead to the problem of freezing at the upper part near to the crucible – the temperature for the TMF 300 Hz down is below the melting point

temperature at the crucible. The absolute temperature value might be not correct because of the missing back coupling to global simulations but the tendency corresponds to the experiences in the experiments.

Now, we discuss the facetted growth in slightly more detail. Kuroda et al. did a geometrical analysis of the side facet in a horizontal cut, taking into account the undercooling ΔT, the radius of the crystal r_X, and the radial component of the temperature gradient G_T^r [8]. The side length d of the facet can be derived as:

$$d \approx 5\, \Delta T / G_T^r. \quad (1)$$

A small value of G_T^r will stabilize a side facet and lead to a large value of d (In figure 1 we have d=38 mm as obtained in experiments). For the TMF of 180 Hz down we get $G_T^r \approx 1.5$ K/cm in the vicinity of the crystal edge. For the TMF of 300 Hz down it is smaller. Equation (1) was derived by assuming a concentric temperature field at the melt surface with $T=T_m$ at the rounded edges and $T=T_m - \Delta T$ at the centre of the facet. The third dimension, i.e. the vertical direction was not taken into account. Some simple geometrical considerations for the vertical direction were made by Brice [9]. He looked for the (vertical) facet length b in a vertical cut when the interface shape is circular with a radius r_i. Then, b is given by

$$b^2 = 2\, \Delta T\, r_i / G_t^i, \quad (2)$$

where G_t^i is the component of the temperature gradient normal to the facet interface. In our case with a growth direction [00$\bar{1}$] we have small {111} facets at the border of the solid/melt interface as it was shown posteriori by SEM and HRTEM for the crystal grown [4]. It can be expected that they play a central role in the growth kinetics due to their highest atomic smoothness (lowest free energy). For these facets b should be small because a large deflection of the interface should be avoided. Thus, we need a large G_t^i, which means a large vertical component of the temperature gradient – the radial component should be small in order to stabilize the {110} side facets. From figure 7 (right) we can see that the vertical component of the temperature gradient G_t^v beneath the crystal is high when applying a TMF down and low when using a TMF up.

For a growth velocity in the range of 1-6 cm/h [4] we expect an undercooling of about ΔT=3-4 K (see [10-12]). Such an undercooling will be reached in 3-4 mm distance from the T_m isoline in the case with TMF down 300 Hz (G_t^v=12 K/cm), in 4.5-6 mm in the case with TMF down 180 Hz (G_t^v=7.5 K/cm) and in 18-24 mm in the case with TMF up 60 Hz (G_t^v=1.9 K/cm). Except for the {111} facet the crystal/melt interface coincides with the T_m isoline. Therefore, in the two cases of TMF down a small {111} facet is stabilized, whereas in the case of TMF up a {111} facet could be only formed if we have a very strong deflection of the interface.

3.2 Experiments The numerical simulations have been performed with the same process parameters as in two real experiments using a TMF down and a TMF up. As it can be expected from the discussion above the crystal grown in the TMF up 60 Hz exhibits a cylindrical shape (see fig. 8 left) whereas the one grown in the TMF down exhibits a quadratic shape (see fig. 8 right).

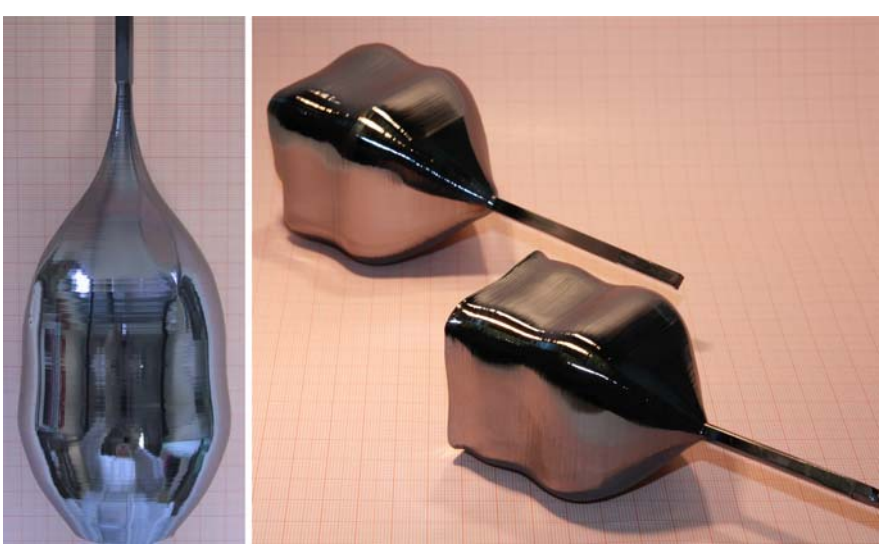

Fig. 8 Crystals grown with TMF up (left) and TMF down (right).

Thus, we demonstrated that the growth of silicon crystal with a nearly-square shaped cross section is possible and understandable by the underlying flow dynamics. Such shape would be of great advantage for the production of silicon for photovoltaic applications, because material loss due to cutting can be significantly reduced. However, another important issue for photovoltaic silicon is the oxygen content, which should be minimized in order to reduce the aging of the solar cells. For two Czochralski runs with the same source material but a TMF up and a TMF down, the measured oxygen content (on interstitials) was 8×10^{17} cm^{-3} in the case of a TMF up and 1.0-1.4$\times10^{18}$ cm^{-3} in the case of a TMF down. The higher contents in the second case can be understood in terms of the melt convection. In figure 9 the time-averaged velocities are shown for the case TMF up 60 Hz in the left part and for the case TMF down 300 Hz in the right part. The source for oxygen in the melt is the dissolution at the crucible walls. In the first case (left) the oxygen is transported mainly along the crucible walls and then to the melt surface, where it can evaporate. In the second case the advective transport is vice versa and the oxygen from the out part is transported near to the crystal/melt interface. Especially, from the bottom there is a (slow) up-stream of oxygen towards the interface.

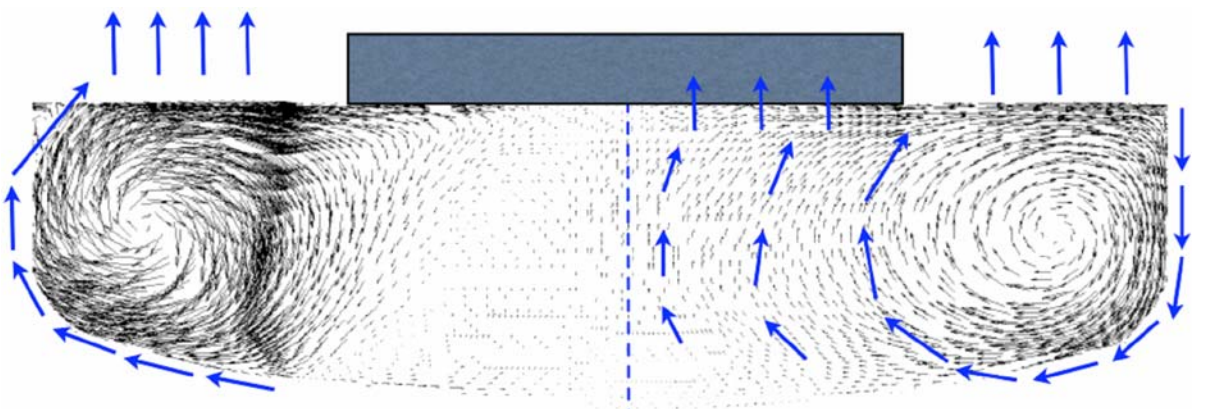

Fig. 9 Time averaged flow field in the case with TMF up (left) and down (right). In the left case the oxygen resolved at the crucible wall is mainly transported along the walls to the melt surface where it evaporates. In the right case the oxygen is transported in the opposite direction and there is a direct flow from the bottom of the melt towards the melt/crystal interface. The large (blue) arrows indicate the preferential transport paths of oxygen.

4 Conclusion

We have performed 3D simulations of melt flow with and without TMF in order to study the temperature distribution in the melt, especially in the vicinity of the melt/crystal interface. We have shown that a TMF down lowers the radial component of the temperature gradient near to the melt surface and increase the vertical component of the temperature gradient below the crystal. This enables the crystal to grow in a square-shaped mode by forming {110} facets. In cases with a TMF up, we expect crystals with cylindrical shape due to the high radial component of the temperature gradient and the low vertical one. Indeed, this corresponds to the results of various Czochralski growth experiments. With a TMF down crystal with nearly square-shaped cross sections were reproducibly grown whereas with a TMF up the crystal shape was cylindrical. On the other hand the oxygen content was slightly larger for crystals grown in TMF down than for those grown in TMF up. However, all investigations were performed still without any optimization of TMF or rotation rates.

Acknowledgements Funding of experiments by CaliSolar is greatfully acknowledged.

References

[1] P. Rudolph, M. Czupalla, and B. Lux, J. Cryst. Growth **311**, 4543 (2009).
[2] O. Klein, C. Lechner, P.-È. Druet, P. Philip, J. Sprekels, C. Frank-Rotsch, F.-M. Kießling, W. Miller, U. Rehse, and P. Rudolph, J. Cryst. Growth **310**, 1523 (2008).

[3] P. Rudolph, J. Cryst. Growth **310**, 1298 (2008).
[4] P. Rudolph, M. Czupalla, B. Lux, F. Kirscht, Ch. Frank-Rotsch, W. Miller, and M. Albrecht, J. Cryst. Growth **318**, 249 (2011).
[5] P. Rudolph, M. Czupalla, N. Dropka, Ch. Frank-Rotsch, F.-M. Kießling, B. Lux, W. Miller, U. Rehse, and O. Root, J. Korean Cryst. Growth Cryst. Technol. **19**, 215 (2009).
[6] M. Kurz, A. Pusztai, and G. Müller, J. Cryst. Growth **198/199**, 101 (1999).
[7] W. Miller, Ch. Frank-Rotsch, and P. Rudolph, J. Cryst. Growth **318**, 244 (2011).
[8] Ekyo Kuroda, Sunao Matsubara, and Tadashi Saitoh, Jap. J. Appl. Phys. **19**, L361 (1980).
[9] J. C. Brice, J. Cryst. Growth **6**, 205 (1970).
[10] K. M. Beatty and K. A. Jackson, J. Cryst. Growth **211**, 13 (2000).
[11] W. Miller, J. Cryst. Growth **325**, 101 (2011).
[12] K. A. Jackson, J. Cryst. Growth **325**, 104 (2011).

